Nanostructures in metastable $GeBi_2Te_4$ obtained by high-pressure synthesis and rapid quenching and their influence on physical properties

Thorsten Schröder,[1] Matthias N. Schneider,[1] Tobias Rosenthal,[1] Andreas Eisele,[1] Christian Gold,[2] Ernst-Wilhelm Scheidt,[2] Wolfgang Scherer,[2] Rico Berthold,[3] and Oliver Oeckler[1,*]

[1]*LMU Munich, Department of Chemistry, Butenandtstraße 5-13 (D), 81377 Munich, Germany*

[2]*Universität Augsburg, Institut für Physik, CPM, 86159 Augsburg, Germany*

[3]*Max-Planck-Institut für Chemische Physik fester Stoffe, Nöthnitzer Strasse 40, 01187 Dresden, Germany*

(Received 7 July 2011; revised manuscript received 7 October 2011; published 14 November 2011)

We report on a new metastable modification of $GeBi_2Te_4$ obtained by high-pressure high-temperature synthesis. It crystallizes in the CuPt type; different nanostructures are induced by various temperature programs under a constant pressure of 12 GPa. The particle size changes from <10 nm in quenched samples to >100 nm for melts slowly crystallized under high pressure. The smaller the domains the more random is their orientation distribution. The nanostructure has a high impact on the temperature characteristics of the electrical resistivity. The domain size determines whether the compounds are metallic or semiconducting. In the latter case the semiconducting behavior is due to the scattering of electrons at domain and/or grain boundaries. Intermediate behavior that starts off metal-like and changes to semiconducting at higher temperature has been observed for samples thermally quenched from the solid state at high pressure. Resistivity measurements of the high-pressure samples involving multiple heating and cooling sequences lead to a significant reduction of internal stress and finally approach a state which is characterized by $\rho(T)$ hysteresis. Our results show the large influence of the domain size and the grain boundary concentration on the properties of the materials and reveal how properties like the thermoelectric figure of merit (ZT) depend on the preparation technique. By the microstructuring of stable $GeBi_2Te_4$, the ZT value drops by one order of magnitude.

DOI: 10.1103/PhysRevB.84.184104 PACS number(s): 61.50.Ks, 61.66.Fn, 64.60.My, 72.15.Jf

I. INTRODUCTION

Tellurides play important roles in various fields of application such as phase-change materials (PCMs) for data storage as well as a broad range of high-performance thermoelectrics. Interestingly, most of the relevant tellurides are not thermodynamically stable. Metastability is, for example, a crucial property of PCMs used in optical as well as electrical rewritable storage devices (DVD-RW, BD-RE, PC-RAM, etc.).[1,2] The recording and erasing process involves the fast and reversible switching between amorphous and metastable disordered crystalline phases with simple average structures which exhibit the A7 (gray arsenic) or the rocksalt structure type. Metastability and disorder are essential to reach extremely short switching times for writing or erasing large amounts of data, as no long-distance diffusion is required and both structural states are inert enough to guarantee reliable long-time data storage. The required material properties of PCMs are, at least in part, similar to those that are crucial in the field of thermoelectrics.[3] However, it remains unclear if the thermoelectric effect itself is important in electrically switchable PCMs.

The long-time goal of most research activities on thermoelectrics, which interconvert thermal and electrical energy, is the generation of electrical energy from waste heat. The efficiency of thermoelectrics depends on the dimensionless figure of merit $ZT = S^2T/\rho\kappa$ (with the Seebeck coefficient S, the electrical resistivity ρ, and the thermal conductivity κ). As all these quantities depend on the charge-carrier concentration, they cannot be optimized independently. The electrical resistivity and the electronic part of the thermal conductivity are inversely proportional to each other according to the Wiedemann-Franz law. Therefore, the only way to decrease the overall thermal conductivity without significantly increasing the electrical resistivity is to influence the phononic part of the thermal conductivity. This can be achieved, for instance, by introducing nanostructures. Phase transitions associated with the formation of long-periodically ordered structures, twinning, or (partial) decomposition may yield nanostructures that scatter phonons rather effectively and therefore enhance the thermoelectric properties. Nanostructures are, of course, metastable states, especially if they are obtained by partial stabilization of highly disordered metastable phases. This can be accomplished by various quenching techniques. However, care must be taken not to completely reach the fully ordered equilibrium state.[4–11]

In addition to the common characteristic feature that the compounds are metastable, many efficient thermoelectrics [e.g., $AgPb_mSbTe_{2+m}$ (LAST),[12] $NaPb_mSbTe_{2+m}$ (SALT),[13] $(AgSbTe_2)_{1-m}(GeTe)_m$ (TAGS),[14] or Bi_2Te_3] contain more or less the same chemical elements in similar ratios as well-known PCMs [e.g., $(GeTe)_n(Sb_2Te_3)$ (GST),[15–17] $Ag_{3.4}In_{3.7}Sb_{76.4}Te_{16.5}$ (AIST)].[18] Inspired by GST-based PCMs in PC-RAM and BD-RE devices, the investigation of the thermoelectric properties of $(GeTe)_{12}Sb_2Te_3$ yielded ZT values of $\sim$1.3 at 450 °C.[3] These compounds exhibit cubic high-temperature phases with Ge, Sb, and vacancies disordered on the cation sites of the rocksalt-type structure, which can be quenched as pseudocubic bulk material. The high ZT value can be related to short-range vacancy ordering effects. Similar metastable rocksalt-type phases of GBT (Ge/Bi/Te) materials have been reported for thin-film samples obtained by sputtering and exhibit rapid phase-change behavior that can be induced by laser irradiation.[19] However, in this case the

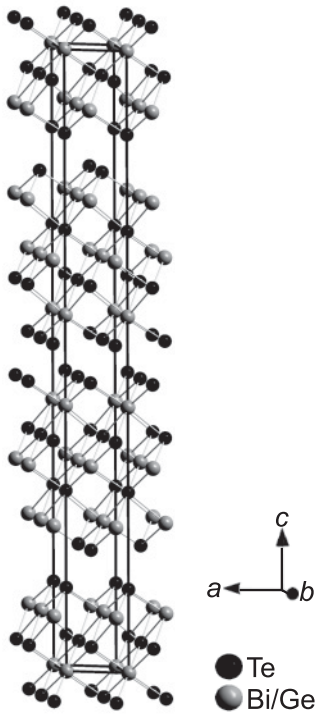

FIG. 1. Crystal structure of stable 21*R*-type $GeBi_2Te_4$ (the small percentage of antisite disorder is neglected).

rocksalt-type phase does not exist as a stable high-temperature phase (it is in fact unstable at any temperature). Therefore, quenching experiments using bulk samples do not yield cubic or pseudocubic phases, but rather the stable rhombohedral layered modifications, which are similar to stable GST phases. Therefore, it is essential to apply methods beyond conventional solid-state synthesis to obtain metastable GBT compounds as bulk materials. Fast quenching methods such as melt-spinning as well as high-pressure experiments seem promising in order to obtain different nanostructures that can be correlated with the corresponding thermoelectric properties.

In this report we focus on $GeBi_2Te_4$, which is one of the peritectic compounds that can be found on the pseudobinary line GeTe-Bi_2Te_3 in the Ge/Bi/Te phase diagram. The stable modification of $GeBi_2Te_4$ crystallizes in a rhombohedral long-range ordered 21*R*-type structure (space group $R\bar{3}m$, no. 166) with 21 hexagonal atom layers in each unit cell (Fig. 1).[20] These 21 layers form three blocks of seven layers each, which can be described as a distorted cutout of the rocksalt-structure type due to the octahedral coordination of the cations. Adjacent blocks are linked via van der Waals gaps by tellurium$\cdots$tellurium interactions. In contrast to this stable phase, the metastable cubic modification found for thin-film sample experiments corresponds to a rocksalt-type structure $(Ge_{0.25}Bi_{0.5}\square_{0.25})Te$ displaying cation defects.[19,21] A phase transition toward the stable state therefore involves a vacancy rearrangement. Layerlike defect ordering and subsequent relaxation leads to the formation of the van der Waals gaps. Intermediate structures between the cubic and the 21*R*-type phases could be observed for $Ge_2Bi_2Te_5$ in annealing experiments on thin films.[22] They involve a shear deformation which may also be important for the phase-change mechanism.

II. EXPERIMENTAL DETAILS

A. Synthesis

Bulk samples with the nominal composition $GeBi_2Te_4$ were prepared by heating a stoichiometric mixture (e.g., 0.3 g) of the pure elements (germanium 99.999%, Sigma Aldrich; bismuth 99.999%, Smart Elements; tellurium 99.999%, Alfa Aesar) in sealed silica glass ampoules to 950 °C under argon atmosphere. The resulting melts were quenched to room temperature in water and used as starting material for the following syntheses. After quenching, some ingots were annealed at 500 °C to obtain the stable 21*R*-type modification.

High-pressure experiments were performed using the multianvil technique with a hydraulic press (Voggenreiter, Mainleus, Germany).[23–26] Quenched $GeBi_2Te_4$ was powdered, loaded into a cylindrical capsule of hexagonal boron nitride (Henze, Kempten, Germany) and sealed with a BN cap. The capsule was centered within two nested graphite tubes, which acted as an electrical resistance furnace. The remaining volume at both ends of the sample capsule was filled with two cylindrical pieces of magnesium oxide. The arrangement was placed into a zirconia tube and then transferred into a pierced Cr_2O_3-doped MgO octahedron (edge length 14 mm, Ceramic Substrates & Components, Isle of Wight, Great Britain). Eight truncated tungsten carbide cubes (truncation edge length 8 mm) separated by pyrophyllite gaskets served as anvils for the compression of the octahedron. Two plates of molybdenum provided electrical contact for the graphite tubes. The assembly was compressed up to a constant pressure of 12 GPa in 350 minutes. At this pressure, three temperature programs were applied (see Table I). Samples were prepared by heating to 850 °C and subsequently (1) quenching the melt by turning off the furnace (melt-quenched samples), or (2) cooling the sample to 200 °C within 5 hours and then turning off the furnace (solid-quenched samples). A third type of high-pressure samples was prepared by (3) cooling the samples to room temperature within 4 hours (slowly cooled samples). After the temperature program the pressure was reduced to ambient pressure within 1050 minutes.

A melt-spinning apparatus (model SC, Bühler, Germany) was used in order to obtain high quenching rates (up to approximately 10^9 K/s) at ambient pressure. Powdered $GeBi_2Te_4$ was loaded into a tantalum blast pipe, which was placed over a rotating copper wheel (60 Hz). Both the tantalum blast pipe and the copper wheel were placed in a recipient, which was evacuated and/or filled with argon. The powder was melted using a water-cooled high-frequency coil (high frequency generator Himmel HIT 12, Himmelwerk Hoch- &

TABLE I. High-pressure sample overview.

Denotation	Pressure	Temperature program
Melt quenched	12 GPa	quenched from melt (850 °C)
Solid quenched	12 GPa	quenched from 200 °C
Slowly cooled	12 GPa	slowly cooled from 850 °C to RT

Mittelfrequenzanlagen GmbH, Germany) and then sprayed onto the rotating copper wheel under an argon pressure of 500 mbar by applying an excess argon pressure connected to the tantalum blast pipe. The melt hits the copper wheel and solidifies immediately. Flat particles with the size of about $5 \times 2 \times 0.2$ mm^3 were hurled away from the wheel onto a collecting tray.

B. Energy dispersive x-ray analysis

Energy dispersive X-ray (EDX) spectra were recorded using a JSM-6500F (Jeol, USA) scanning electron microscope with EDX detector (model 7418, Oxford Instruments, Great Britain). For each particle or fragment of the ingot, respectively, the results of five point analyses were averaged and the error limits were estimated from their variance.

C. X-ray Diffraction

X-ray powder patterns were recorded with a Huber G670 Guinier camera equipped with a fixed imaging plate and integrated read-out system using Cu-$K_{\alpha 1}$ radiation (Ge monochromator, $\lambda = 1.54059$ Å). Specimens were prepared by crushing representative parts of the samples and fixing the powder on Mylar foils using silicone grease. Low-temperature measurements between 10 and 300 K were obtained using a cryo cooling system (Cooling head, CTI-Cyrogenics, model 22 CP). The phase homogeneity was assessed and lattice parameters were determined by pattern fitting (Rietveld method) using the program TOPAS.[27] Temperature-dependent powder-diffraction experiments at temperatures above 300 K were performed with a STOE Stadi P powder diffractometer equipped with an imaging plate detector system using Mo-$K_{\alpha 1}$ radiation (Ge monochromator, $\lambda = 0.71093$ Å) in Debye–Scherrer geometry. Powdered specimens were filled into silica glass capillaries with 0.3 mm diameter and sealed with silicone grease under argon atmosphere. During the measurement, the samples were heated up to 600 °C in a graphite furnace and then cooled to room temperature with a heating/cooling rate of 5 K/min.

D. Transmission electron microscopy

For transmission electron microscopy studies, finely ground samples were dispersed in ethanol and distributed on copper grids coated with a holey carbon film (S166-2, Plano GmbH, Germany). The grids were fixed on a double tilt holder. Selected area electron diffraction (SAED) and high resolution transmission electron microscopy (HRTEM) were done on a JEM2011 (Jeol Ltd., Japan) with a tungsten thermal emitter and an acceleration voltage of 200 kV equipped with a TVIPS CCD (model 114, resolution: 1k × 1k). Further HRTEM, SAED, and EDX measurements were done on a Titan 80-300 (FEI, USA) with a field-emission gun operated at 300 kV equipped with a TEM TOPS 30 EDX spectrometer (EDAX, Germany). Images were recorded using an UltraScan 1000 camera (Gatan, USA, resolution 2k × 2k). HRTEM and SAED data was evaluated using the Digital Micrograph and EMS software;[28,29] for STEM and EDX data the program ES Vision was used.[30]

E. Electrical and thermal transport measurements

The temperature dependent resistivity $\rho(T)$ of various stable and metastable $GeBi_2Te_4$ modifications were measured by a standard four-probe dc method employing a constant current of 5 mA and using a physical property measurement system (PPMS, Quantum Design). The data were collected in the temperature range of 2–300 K by cooling and heating sequences in which the temperature changed at a rate of 0.5 K/min. The uncertainty of the absolute electrical resistivity values (approximately 20–30%) has been estimated by taking into account the errors in specifying the sample dimensions.

The thermoelectric power $S(T)$ and the thermal conductivity $\kappa(T)$ of samples crystallizing in the stable $GeBi_2Te_4$ modification were measured simultaneously using the commercial thermal transport option of the PPMS. This is based on a relaxation method employing one heater and two thermometers to determine the induced thermal voltage and the temperature gradient along the sample in a temperature range between 4 and 300 K. These measurements were carried out using bar-shaped samples with typical dimensions of about $1 \times 2 \times 5$ mm^3 during a heating process at a rate of 0.5 K/min. The total accuracy of $S(T)$ and $\kappa(T)$ is about 5%.

III. RESULTS AND DISCUSSION

A. Structure of quenched HP-$GeBi_2Te_4$

The powder diffraction pattern of a sample obtained by quenching the melt of $GeBi_2Te_4$ under a constant pressure of 12 GPa (i.e., switching off the furnace) could be indexed assuming a rhombohedral unit cell with $a = 4.3508(3)$ Å and $c = 11.234(2)$ Å. Starting from an α-GeTe-type structure model (space group $R3m$), which allows many degrees of freedom, Ge, Bi, and vacancies were placed on the cation position (occupancy factors 0.25 for Ge and 0.5 for Bi) and Te (fully occupied) on the anion position. The occupancy factors were derived from the nominal composition, which is confirmed by the EDX results (for all $GeBi_2Te_4$ samples between $Ge_{0.9(1)}Bi_{2.2(1)}Te_4$ and $Ge_{1.1(1)}Bi_{2.0(1)}Te_4$). The Rietveld refinement (shown in Fig. 2) turned out that there is no evidence

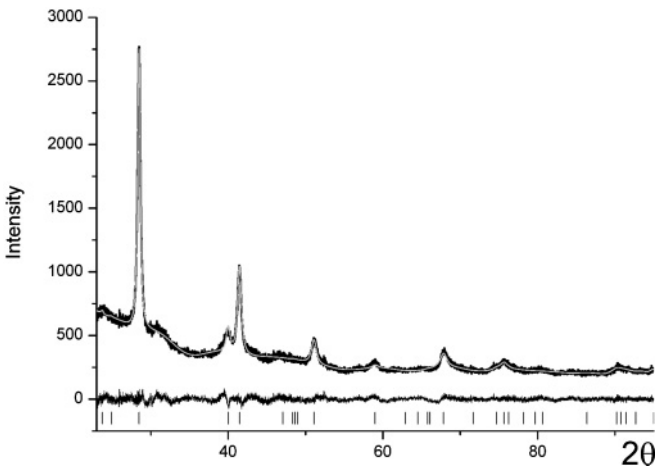

FIG. 2. Rietveld refinement of melt-quenched HP-$GeBi_2Te_4$: experimental powder pattern (black), calculated pattern (gray), difference plot (black), and tick marks (black, straight lines).

TABLE II. Crystal data and Rietveld refinement of melt-quenched $GeBi_2Te_4$.

Sum formula	$GeBi_2Te_4$
Molar mass (in g/mol)	1000.97
Lattice parameters (in Å)	$a = 4.3508(3)$ Å; $c = 11.234(2)$
Cell volume (in Å^3)	184.16(5)
Radiation	Cu-$K_{\alpha 1}$ ($\lambda = 1.54059$ Å)
Density (in g/cm^3)	6.769(2)
Space group	$R\bar{3}m$ (no. 166)
2 theta range	$22^\circ < 2\Theta < 95^\circ$
Number of reflections	32
Refined parameters	12 structural/36 background
Constraints	2
Profile function	fundamental parameter approach
Step width (2Θ)	0.005°
R_{wp}; R_p	0.0135; 0.0104

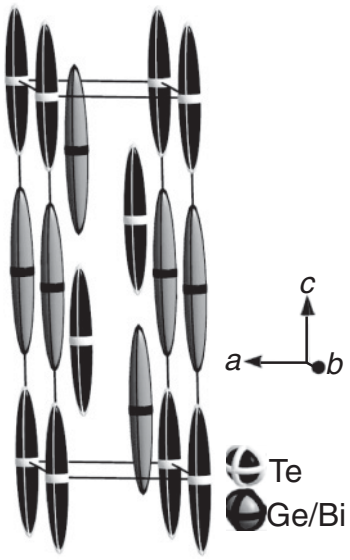

FIG. 3. "Average" structure model of metastable HP-$GeBi_2Te_4$, as determined from Bragg data (displacement ellipsoids for 99% probability).

for noncentrosymmetry of the average structure, as in contrast to α-GeTe, all cation-anion distances are equal within two standard deviations. Therefore, the average structure seems not to be layered, and the space group can be identified as $R\bar{3}m$ (no. 166). Details of the Rietveld analysis and the refined atomic parameters are given in Tables II and III, respectively.

The average structure model derived from Bragg reflections corresponds to the CuPt-type structure, a rhombohedrally distorted variant of the rocksalt type, derived from the latter by stretching the unit cell along ⟨111⟩. In fact the powder pattern contains no significant evidence for different scattering densities on anion and cation positions, as disordered germanium, bismuth, and vacancies lead to an average electron count of 49.5 at the cation position, and tellurium involves 52 electrons on the anion position. Thus, the structure might formally be described assuming the α-Hg type with just one Wyckoff position for all atoms, however, electron-diffraction patterns clearly show the CuPt type's reflections *hkl* with $h, k, l = 2n + 1$ whose intensity (similar to the rocksalt case) can only be observed in case of different scattering densities for cation and anion sites (see the next section). Of course, a certain degree of antisite disorder cannot be excluded; however, such phenomena have been thoroughly investigated for Ge/Sb/Te phases, where the amount of antisite disorder is either very small or not significant.[17,31] Although the refinement fits the experimental data, the structure model does not correspond to an ordered compound, and the disorder goes far beyond the cation disorder itself. The "average" structure from Bragg data can only be described with very prolate atomic displacement ellipsoids, as can be seen in Fig. 3; so in fact there is no average structure with, at least in part, "normal" atom positions. These results suggest that a cubic rocksalt-type phase is formed under high pressure but partially relaxes to a layered trigonal structure as soon as the pressure is released. The short-range order in this phase may locally correspond to the structure of the stable room temperature phase. Obviously, the high vacancy concentration of 25% on the cation sites does not allow a completely random vacancy distribution at ambient conditions.

The powder-diffraction patterns of the slowly cooled and solid-quenched samples, respectively, do not differ significantly from those of samples that were quenched from the melt, although the micro/nanostructures are significantly different (see subsequent discussion). However, Table IV shows that the lattice parameters of the average structures vary slightly. All trigonal *c*/*a* ratios are almost equally far from that of the trigonal setting of a unit cell with cubic metrics (2.45).

Figure 4 shows that temperature-dependent powder-diffraction experiments and *ex-situ* annealing of high-pressure samples (for 36 hours at 300 °C) prove that the high-pressure phase is metastable at ambient pressure. The reflections of the layered 21*R*-type structure reappear when the metastable compound is heated over 200 °C.

B. Nucleation mechanism and nanostructuring

The nanostructure of the melt-quenched sample, which is shown in Fig. 5(a), is characterized by a broad range of different domain orientations with domain sizes <10 nm. The domains are intergrown, but there are no coherent

TABLE III. Atom positions and displacement parameters of HP-$GeBi_2Te_4$.

Atom	Wyck.	*x y z*	s.o.f.	U_{eq}	$U_{11} = U_{22} = 2U_{12}$	U_{33}	$U_{13} = U_{23}$
Te	3*a*	0 0 0	1	0.15(2)	0.017(11)	0.48(7)	0
Bi/Ge	3*b*	0 0 1/2	Bi 0.5 Ge 0.25	0.18(2)	0.008(11)	0.43(6)	0

TABLE IV. Comparison of the lattice parameters of various high-pressure samples (cf. text).

Denotation	a (Å)	c (Å)	c/a	Volume (Å^3)
Melt quenched	4.3508(3)	11.234(2)	2.582	184.05(5)
Solid quenched	4.347(2)	11.184(5)	2.573	183.1(2)
Slowly cooled	4.3495(5)	11.043(3)	2.539	180.93(7)

domain walls. Therefore, the SAED pattern corresponds to the combination of multiple patterns and not to a single crystallite. A few grains with larger domains can be found, but they are rare exceptions. Thus, quenching the melt under a high constant pressure leads to nucleation dominated growth.

The solid-quenched sample exhibits larger and more anisotropic domains with average dimensions $\geqslant$10 nm. Therefore, it is possible to obtain single crystalline SAED patterns, as shown in Fig. 5(b), if larger domains are selected. These patterns contain reflections hkl with $h, k, l = 2n + 1$, which implies that there are different scattering densities for anion and cation sites, respectively. There are no pronounced diffuse streaks in the SAED patterns. Thus, there is no pronounced intermediate-range order corresponding to extended vacancy layers or van der Waals gaps within the domains as they are known from the stable trigonal phases. Probably the lack of vacancy ordering limits the maximal domain size as vacancies might aggregate at domain boundaries. The crystallites are larger than the ones in the melt-quenched HP sample; yet, the domains are still randomly oriented. The domain shape is more anisotropic than in the melt-quenched sample.

Figure 5(c) shows that the slowly cooled sample has large crystallites $\geqslant$100 nm. Twinned areas next to single-domain areas can be observed. All slowly cooled samples exhibit extended vacancy layers that lead to van der Waals gaps if the adjacent Te atom layers relax. Therefore, diffuse streaks can be observed in the corresponding SAED patterns. These large domains indicate fast growth crystallization rather than nucleation dominated growth. The relative orientation of the twin domains corresponds to the ⟨111⟩ directions of a pseudocubic structure. This corroborates the assumption that there is a cubic high-pressure phase of $GeBi_2Te_4$ which, upon a phase transition toward a trigonal phase, involves fourfold twinning according to the *translationengleiche* cubic → rhombohedral group-subgroup relationship.

The powder X-ray diffraction (PXRD) pattern of melt-spun $GeBi_2Te_4$ corresponds to that of the ordered 21R-type structure and not to the PXRD patterns of the high-pressure samples. Yet, melt-spun $GeBi_2Te_4$ exhibits small intergrown domains, the smallest ones with a diameter of ∼10 nm, as shown in Fig. 6. Larger domains are also present. The domain orientation changes within one grain, however, not as randomly as in the quenched high-pressure samples.

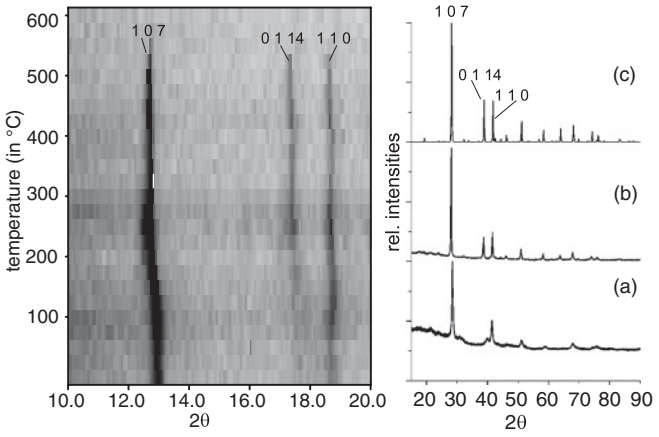

FIG. 4. Temperature-dependent PXRD [left, room temperature to 600 °C, Mo-$K_{\alpha 1}$ radiation intensity from 0 (white) to maximum (black)] of the melt-quenched HP phase; PXRD (Cu-$K_{\alpha 1}$ radiation) of the melt-quenched sample (right): (a) as removed from the press, (b) after annealing for 36 h at 300 °C, (c) calculated powder pattern of 21R-type $GeBi_2Te_4$.

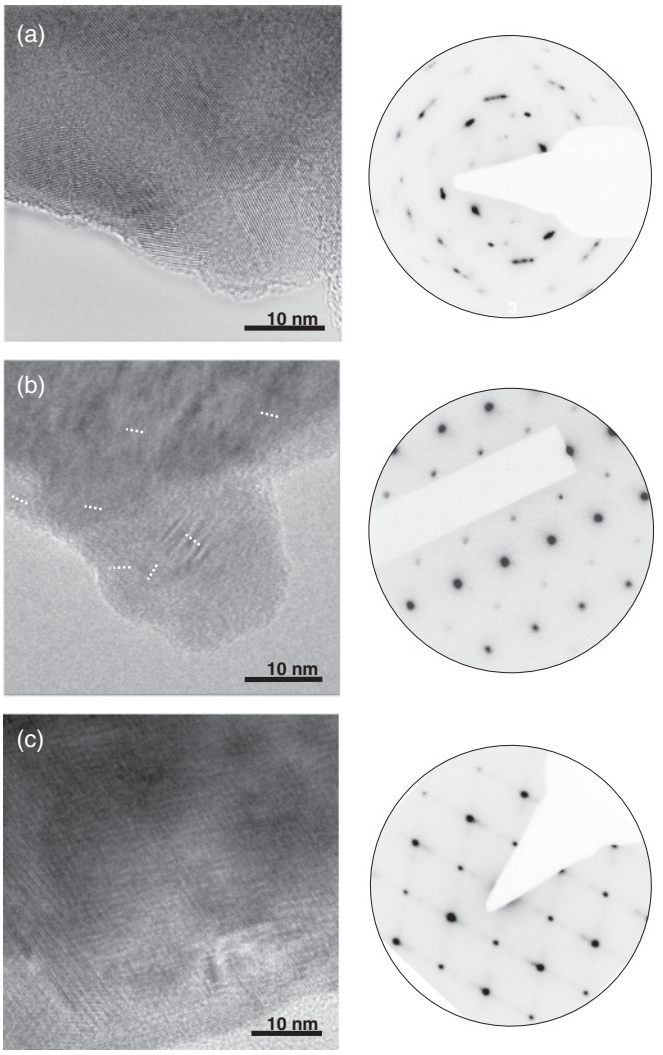

FIG. 5. HRTEM images (left) and the corresponding SAED (right) (a) of the melt-quenched sample (Titan 80–300); (b) of the solid-quenched sample, some domain orientations are highlighted with white dashed lines (JEM 2011); (c) of the slow-cooled sample: here different domain orientations overlap (Titan 80–300).

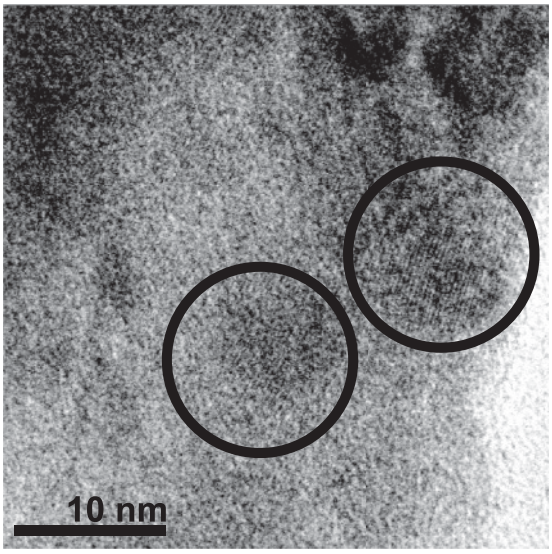

FIG. 6. HRTEM image of a melt-spun sample of $GeBi_2Te_4$; two well-ordered domains of the stable-layered phase are highlighted by black circles.

C. Influence of the nanostructure on the electrical resistivity

The following section conduces to the understanding of the influence of the nanostructure of the metastable modifications of HP-$GeBi_2Te_4$ on the temperature-dependent resistivity ρ(T). Therefore the resistivity of three different metastable quenched samples—slowly cooled, solid-quenched, and melt-quenched—were synthesized and compared with an annealed ingot as well as a melt-spun particle, both crystallizing in the stable modification.

1. Stable and melt-spun modification of $GeBi_2Te_4$

The resistivity of an annealed ingot of the stable ambient-pressure modification of $GeBi_2Te_4$ is plotted vs temperature in the range between 2 and 300 K in Fig. 7(a). The decrease

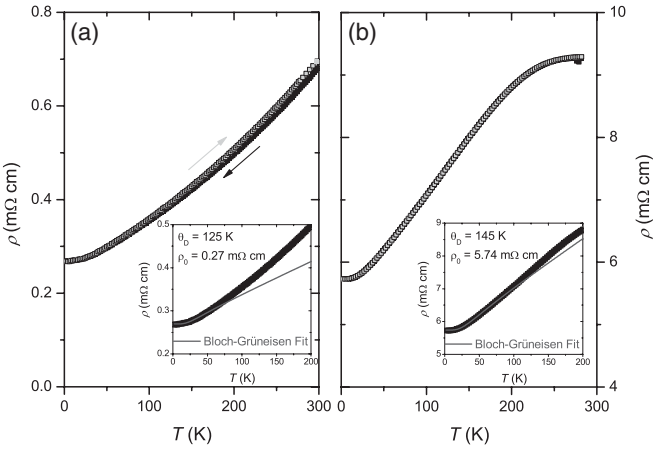

FIG. 7. Comparison of the temperature-dependent resistivity of (a) an annealed ingot of 21*R*-type $GeBi_2Te_4$ and (b) a melt-spun particle of $GeBi_2Te_4$. The inserts show the low-temperature behavior together with a fit according to the Bloch-Grüneisen relationship (solid line). The arrows denote cooling and heating sequences, respectively.

of $\rho(T)$ with decreasing temperature suggests metal-like behavior. However, the high residual resistivity ρ_0 of about 0.3 mΩ cm together with the small residual resistivity ratio of RRR $= \rho(300\,\mathrm{K})/\rho(2\,\mathrm{K}) = 2.52$ suggest the presence of severe disorder. The metallic conductivity behavior depends on two different scattering processes. The temperature-independent residual resistivity ρ_0 originates from the scattering of conduction electrons by defects (impurity atoms, grain boundaries, etc.). In the present case this is probably due to the Ge/Bi disorder at the cation sites. The second—temperature-dependent—process is due to the scattering of conduction electrons by phonon excitations. These two processes yield the description of simple metals via the Bloch-Grüneisen (BG) relation

$$\rho_{\mathrm{BG}}(T) = \rho_0 + \frac{4B}{\Theta_D}\left(\frac{T}{\Theta_D}\right)^5 \int_0^{\Theta_D/T} \frac{z^5 \mathrm{d}z}{(e^z - 1)(1 - e^{-z})}$$

where B is the temperature-independent electron-phonon interaction strength, Θ_D the Debye-temperature, and $z = \hbar\omega/k_BT$.

The insert of Fig. 7(a) depicts the resistivity behavior $\rho(T)$ of the stable $GeBi_2Te_4$ modification in comparison with a corresponding data fit employing the BG relationship. The BG relation fits the experiment sufficiently well only at temperatures below ∼40 K. For higher temperatures, $\rho(T)$ displays larger values than those expected by the BG relation for metallic behavior. This suggests an onset of semiconducting behavior at elevated temperatures in accordance with the high residual resistivity and the small RRR value. Furthermore, $\rho(T)$ of the annealed ingot reflects fully reversible behavior between cooling and heating sequences only below 40 K in the region where experimental data can be fitted by the BG relation. This reversibility can also be retrieved in the metastable modifications of $GeBi_2Te_4$ (see subsequent discussion).

The deviation from metallic behavior above a certain temperature becomes more evident in the resistivity of the melt-spun particle [see Fig. 7(b)], although in this case the BG relation fits the experimental data well up to ∼60 K. However, the residual resistivity ρ_0 increases by a factor of 20 in comparison to the annealed ingot. Furthermore, $\rho(T)$ of the melt-spun particle starts to saturate already at ∼9.3 mΩ cm in the high-temperature regime. The higher resistivity can be attributed to the reduction of the grain size (up to 10 nm) and can therefore be related to the increasing number of domain and grain boundaries acting as scattering centers. The saturation below room temperature is in line with a transition from metal-like to a degenerate semiconducting behavior, as supported by the description via the BG formalism [see insert Fig. 7(b)] at low temperatures, which also takes the temperature dependency of the charge carrier density into account.[32] Such a two-regime behavior was recently reported for Ge-based clathrate I compounds as well as Sb-based skutterudites.[33–35]

These results point out that the nanostructure, e.g., the domain size and the relative orientation, influence the temperature characteristics of the resistivity behavior even if the crystal structure is maintained (21*R* type).

2. Metastable quenched HP-$GeBi_2Te_4$

All three high-pressure samples are characterized by pronounced irreversible temperature dependencies of $\rho(T)$ for

repeated cooling and heating cycles in the temperature range between 44 and 260 K. This is shown for the slowly cooled sample of HP-$GeBi_2Te_4$ in Fig. 8. There is a drastic change of the hysteretic behavior when the $\rho(T)$ sequences of cycle one and two are compared. However, already after the third cooling/heating sequence the hysteresis curves remain rather invariant. There is, however, a subtle decrease of the resistivity [and of the $\rho(T)$ minima at ca. 35–38 K] with increasing number of cooling/heating cycles.

In the final state after more than three successive cooling and heating sequences, the resistivity $\rho(T)$ shows a metal-like behavior above 35 K and an insulating one for lower temperatures, similar to the behavior observed, e.g., for didymium skutterudites $(Pr,Nd)(Fe,Co)_4Sb_{12}$ and $(Pr,Nd)(Fe,Ni)_4Sb_{12}$.[36] Below 44 K heating and cooling curves show reversibility, while above 44 K a hysteresis with a maximal splitting of 0.014 mΩ cm at ∼208 K occurs. One may speculate that the $\rho(T)$ behavior in the reversible regions is mainly controlled by the intrinsic resistivity of the grains, whereas above 44 K the resistivity of the grain boundaries starts to dominate, as observed in the case of the stable $GeBi_2Te_4$ modification [see previous discussion, Fig. 7(a)].

In Fig. 9 the temperature-dependent resistivity behavior of three metastable high-pressure samples of $GeBi_2Te_4$ obtained by different cooling/quenching procedures is compared. All three samples are characterized by a hysteretic $\rho(T)$ behavior, which also depends on the number of cooling/heating sequences applied (vide supra; Fig. 8). However, in order to study exclusively the competition between the intrinsic resistivity of the domains with that of the grain boundaries, only those $\rho(T)$ cooling/heating curves were depicted in Fig. 9, which remained invariant after several measuring cycles. All of the three samples possess reversible temperature dependence below ∼40 K. Above that temperature, the temperature characteristics of the resistivity changes from metallic-like (slowly cooled) to semiconducting (melt-quenched sample). Hence, the temperature-dependent resistivity behavior critically depends on the sample history, especially on the cooling/quenching approach applied. In contrast the hysteretic

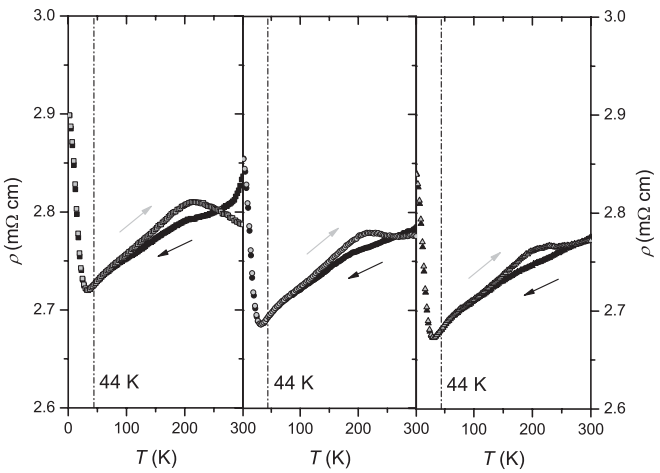

FIG. 8. Temperature-dependent resistivity of a slowly cooled HP-$GeBi_2Te_4$ sample. From left to right three successive cooling (black) and heating (gray) sequences, approaching a final state.

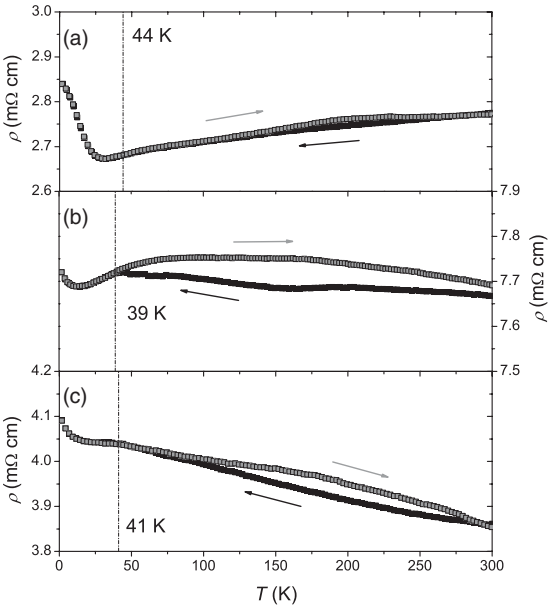

FIG. 9. Final state of the cooling (black) and heating (gray) sequences of the temperature-dependent resistivity of (a) slowly cooled, (b) solid-quenched, and (c) melt-quenched high-pressure samples of $GeBi_2Te_4$.

behavior above 40 K remains a characteristic feature of all the three different samples.

The occurrence of such hysteresis effects could be due to either a first-order phase transition or the presence of internal stress. A first-order phase transition can be excluded based on temperature-dependent x-ray experiments, which do not reveal any significant change in the powder-diffraction pattern down to 15 K (except for a trivial change of lattice parameters), as well as by specific heat studies (not shown here), which do not indicate any phase transformation. Therefore, the hysteretic $\rho(T)$ behavior is probably due to the internal stress of the grains. The extent of the hysteresis changes drastically with an increasing domain size and the number of their relative orientation in the different samples. Accordingly, the slowly cooled sample is characterized by the smallest hysteresis splitting of all three samples [see Fig. 9(a)]. This is consistent with the expected small change of internal stress as a consequence of the large domain size ($\geqslant$100 nm) and the presence of only few domain orientations, as evidenced by the HRTEM studies. A similar, but more pronounced splitting is therefore found in case of the melt-quenched sample [see Fig. 9(c)], which is characterized by very small particles ($<$10 nm) showing many different orientations. However, the solid-quenched sample reveals the strongest splitting of all metastable $GeBi_2Te_4$ compounds [see Fig. 9(b)]. This is probably a result of the strongly anisotropic size of the grains.

Due to this type of nanostructuring, the total resistivity of these samples is not only affected by the intrinsic structure and disorder of the domains but also by a contribution of the microscopic nature of the domain and/or grain boundaries. The change of the residual resistivity in Fig. 9 suggests that also the dominant scattering mechanisms might differ in the three samples. The slowly cooled high-pressure sample exhibits the lowest residual resistivity and the most

pronounced similarity to the stable modification [e.g., metallic conductivity at ambient temperature; see Fig. 7(a)]. This is basically due to the fact that this sample exhibits the largest domains of the three high-pressure systems and displays a disordered pseudocubic-layered structure. The melt-quenched sample, however, shows semiconducting behavior between 41 K and room temperature in spite of the isotropy and rather random orientation of its domains. The temperature dependence of the resistivity is therefore dominated by the grain boundaries' contributions. The solid-quenched sample indicates the highest residual resistivity of all the high-pressure species under investigation. This remarkably high value in combination with the pronounced grain anisotropy implies a coexistence of both scattering mechanisms discussed (see previous discussion). The $\rho(T)$ behavior of the solid-quenched modification, however, marks an intermediate behavior and thus adopts to the low-temperature behavior of the slowly cooled and mimics the high-temperature behavior of the melt-quenched one.

D. Influence of grain boundaries on *ZT*

In order to investigate the influence of the sample preparation techniques on the thermoelectric figure of merit *ZT*, the thermal and electrical transport properties of three characteristic samples were measured between 4 K and room temperature. In this respect the annealed ingot of stable 21*R*-type $GeBi_2Te_4$ represents a benchmark sample, which is compared with two pellet samples (samples two and three). Sample two is a pellet pressed of 21*R*-$GeBi_2Te_4$ powder, while the third sample is a pellet composed of cold-pressed powder of the melt-spun 21*R*-$GeBi_2Te_4$. It was not possible to perform such measurements with the high-pressure samples due to their small sample volumes.

A comparison of the $\rho(T)$ behavior of these three samples is plotted in Figs. 10(a)–10(c). The $\rho(T)$ behavior of the annealed ingot and that of the melt-spun sample were already characterized as metal-like in Fig. 7. In contrast, $\rho(T)$ of the two pellets do not show metal-like conductivity behavior. In addition, ρ_0 increases by a factor of about 30 and 60 in the case of both pellet samples, irrespective of the sample's origin (stable modification or melt-spun 21*R*-$GeBi_2Te_4$ sample, respectively). Two closely related control parameters might be responsible for observation of semiconducting behavior, namely the nano- or microstructure formation by different synthesis routes and the process of pellet pressing itself. Both lead to an increasing number of grain boundaries and therefore trigger the increase of ρ_0 and the change of the $\rho(T)$ behavior.

These observations are consistent with the thermal conductivity $\kappa(T)$ behavior shown in Figs. 11(a) and 11(b). The total thermal conductivity κ_{total} of solids can be expressed as the sum of an electrical κ_{el} as well as a phononic κ_{ph} contribution. The electrical contribution was estimated from the electrical resistivity (cf. Fig. 10) via the Wiedemann-Franz law. Subtracting this part from the experimentally determined total thermal conductivity yields the phononic contribution.

In Fig. 11(a) κ_{total} of the annealed ingot of the stable modification is composed of significant contributions from κ_{ph} and κ_{el}. While at room temperature both parts coexist and

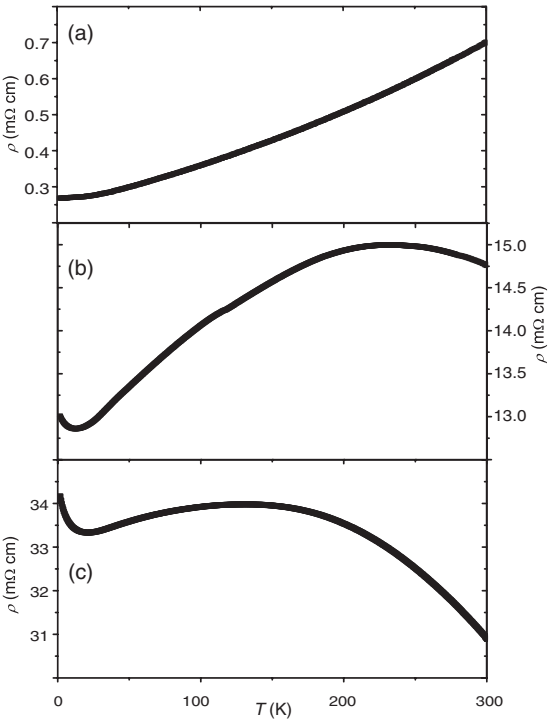

FIG. 10. Comparison of the temperature-dependent resistivity ρ(T) (heating from 2 to 300 K) of (a) an annealed ingot of $GeBi_2Te_4$, (b) a pressed powder pellet of 21*R*-$GeBi_2Te_4$, and (c) a pressed powder pellet of melt-spun $GeBi_2Te_4$.

contribute approximately by the amount to κ_{total}, a phonon-dominated state is observed below 50 K. The maximum of κ_{ph} at about 13 K displays the onset of phonon umklapp scattering which effectuates a decrease of κ_{ph} above a certain temperature. Such kind of maximum depends only weakly on the Debye temperature and occurs well below $\Theta_D/10$. The low-temperature slope of κ_{ph} thus indicates defect scattering and becomes large when the number of defects is small.

A comparison with the $\kappa(T)$ results of the two pellets indicate an overall and significant reduction of $\kappa_{total}(T)$ [Fig. 11(b)]. Generally, κ_{ph} of the thermal conductivity of both samples follows the pattern of κ_{total} while the κ_{el} contribution vanishes, as expected in light of the high resistivity values observed. Furthermore, the change of the low-temperature slope of κ_{ph} hints to an increase of phonon scattering at boundaries and/or point defects. Hence, the reduced thermal conductivity of the pellet-pressed samples originates mainly from the enhancement of these scattering processes.

The thermopower $S(T)$ of the three samples is depicted in Fig. 11(c). For the annealed ingot of the stable modification, an increase of the thermopower up to about $+50$ μV/K at room temperature can be observed. The positive sign of $S(T)$ between 4 and 300 K reveals the characteristic behavior of a *p*-type material. The featureless, almost linear temperature dependence of $S(T)$ indicates the absence of any significant correlations within the charge carriers and is expected for the diffusion thermopower above the Debye temperature (125 K).

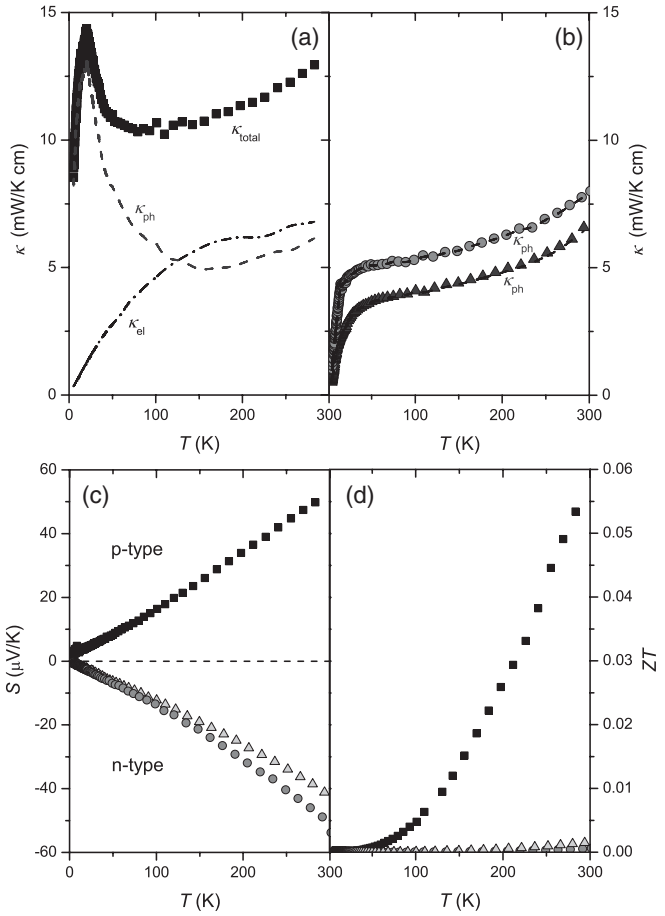

FIG. 11. Temperature characteristics of (a) the total thermal conductivity κ_{total} (black squares), the phonon contribution κ_{ph} (dashed line), and electronic contribution κ_{el} (dashed and dotted line) for the annealed ingot of $GeBi_2Te_4$; (b) κ_{total} for the pressed-powder pellet of 21*R*-type $GeBi_2Te_4$ (gray circles) and the powder pressed pellet of melt-spun $GeBi_2Te_4$ (gray triangles) and the phonon contributions (dashed lines, dark gray); (c) the Seebeck coefficient; and (d) the *ZT* value for the annealed ingot (black squares), the pressed-powder pellet of 21*R*-type $GeBi_2Te_4$ (gray circles), and the pressed-powder pellet of melt-spun $GeBi_2Te_4$ (light gray triangles).

In this temperature region electron-phonon scattering is the dominant-scattering mechanism and given by

$$S_d(T > \Theta_D) = \frac{\pi^2 k_B^2 2m_e}{|e|\hbar^2(3n\pi^2)^{2/3}} \cdot T,$$

with $k_B = 1.38065 \cdot 10^{-23}$ J/K, $m_e = 9.109\,38 \cdot 10^{-31}$ kg, $e = 1.602\,18 \cdot 10^{-19}$ C, and $h = 6.626\,07 \cdot 10^{34}$ Js. According to this equation, the slope below 300 K yields a density of charge carriers of $3.4 \cdot 10^{21}$ cm^{-3}.

In contrast to its influence on $\rho(T)$ and $\kappa(T)$, the method of synthesis has no drastic influence on $S(T)$ except for the remarkable change of sign in the thermopower of the pellets from positive (*p*-type) to negative (*n*-type). The absolute values of $S(T)$, as well as the carrier concentration ($\sim 10^{21}$ cm^{-3}) of the pellet samples, remain more or less the same.

The *ZT* values for the three samples calculated from the present results are shown in Fig. 11(d). For the annealed ingot of the stable modification a *ZT* value of 0.055 was reached at room temperature. The *ZT* values of both pellet samples were found to be one order of magnitude lower, which disqualifies these sample from thermoelectric applications. Significant scattering of the charge carriers on grain boundaries results in high resistivity values for the micro- or nanostructured samples and, as a consequence, in a small electronic contribution to the thermal conductivity.

IV. CONCLUSION

Quenching melts of $GeBi_2Te_4$ at high pressure yields metastable samples whose average structure is related to the rocksalt type, similar to samples obtained by laser irradiation of thin films for PCM applications. Partial relaxation toward the stable trigonal-layered modification leads to a rhombohedrally distorted crystal structure. The metastable state can be completely relaxed by annealing. Concerning PCMs, the nucleation mechanisms are important. "Nucleation-dominated growth" begins spontaneously at different spots in the amorphous phase and therefore leads to a multitude of grains, which have no crystallographic relation to each other. We have shown that the crystallization of melts during rapid quenching is very similar; an intermediate solid amorphous phase might be discussed for bulk samples as well but cannot be confirmed by our experiments. The domain size and therefore probably the nucleation mechanism depends on the temperature regime, including quenching rates, which were applied under a constant pressure of 12 GPa. The nanostructures obtained and especially the corresponding domain and grain boundaries have a large influence on the temperature characteristics of the electrical resistivity. In the high-pressure compounds the characteristics of the electrical resistivity changes from metal-like to semiconducting behavior with decreasing domain size and more randomly oriented domains, because the resistivity becomes more dominated by scattering of the electrons at the domain or grain boundaries. The temperature regime during the synthesis therefore determines at which temperature this type of scattering becomes dominant. However, multiple heating and cooling sequences in the course of the resistivity measurements show that the system seems to approach a final state. Apparently, internal stress needs to be reduced before the measurements yield invariant $\rho(T)$ sequences but even after the stabilization a hysteretic behavior remains.

As a consequence, the preparation technique has a large influence on the *ZT* value, as shown by measurements on samples that exhibit the stable-layered structure. The thermal conductivity is influenced by the electronic contribution, which decreases significantly in pressed pellets with many grain boundaries; however, it is accompanied by the corresponding increase of the electrical resistivity. Therefore, the *ZT* value drops by more than an order of magnitude because the phononic contribution becomes dominant. These findings illustrate the importance of the thermal conditioning of thermoelectrics, especially in order to ensure sufficient electrical conductivity. It is often difficult to reproduce thermoelectric materials with distinct properties because different methods of synthesis (like hot press, high-pressure experiments, or conventional solid-state preparation techniques), annealing

times, and temperatures lead to various amounts of grain boundaries and therefore strong deviations in *ZT*.

ACKNOWLEDGMENTS

We thank T. Miller and M. Rotter for the temperature-dependent powder-diffraction experiments, C. Minke for SEM operation and EDX analyses, and M. Döblinger for help with TEM operation. We are indebted to G. Kreiner for providing access to the melt-spinner and gratefully acknowledge W. Schnick's generous support of this work. This investigation was funded by the Deutsche Forschungsgemeinschaft (grants OE530/1-2 and SCHE487/12-1) and the Studienstiftung des deutschen Volkes.

*Correspondence author: oliver.oeckler@gmx.de

[1] W. Bensch and M. Wuttig, Chem. Unserer Zeit **44**, 92 (2010).
[2] S. Raoux, Annu. Rev. Mater. Res. **39**, 9 (2009).
[3] M. N. Schneider, T. Rosenthal, C. Stiewe, and O. Oeckler, Z. Kristallogr. **225**, 463 (2010).
[4] J. Sommerlatte, K. Nielsch, and H. Böttner, Phys. J. **6**, 35 (2007).
[5] A. Bulusu and D. G. Walker, Superlattices Microstruct. **44**, 36 (2008).
[6] A. Majumdar, Science **303**, 777 (2004).
[7] M. S. Dresselhaus, G. Chen, M. Y. Tang, R. Yang, H. Lee, D. Wang, Z. Ren, J.-P. Fleurial, and P. Gogna, Adv. Mater. **19**, 1 (2007).
[8] D. L. Medlin and G. J. Snyder, Curr. Opin. Colloid Interface Sci. **14**, 226 (2009).
[9] M. G. Kanatzidis, Chem. Mater. **22**, 648 (2010).
[10] Y. C. Lan, A. J. Minnich, G. Chen, and Z. F. Ren, Adv. Funct. Mater. **20**, 357 (2010).
[11] J. R. Sootsman, D. Y. Chung, and M. G. Kanatzidis, Angew. Chem. Int. Ed. **48**, 8616 (2009).
[12] A. C. Bruce, J. K. Matthew, L. H. Joel, H. Mi-Kyung, C. Duck-Young, and G. K. Mercouri, Adv. Funct. Mater. **19**, 1254 (2009).
[13] P. F. P. Poudeu, J. D'Angelo, A. D. Downey, J. L. Short, T. P. Hogan, and M. G. Kanatzidis, Angew. Chem. Int. Ed. **45**, 3835 (2006).
[14] F. D. Rosi, J. P. Dismukes, and E. F. Hockings, Electron Eng. **79**, 450 (1960).
[15] T. Matsunaga and N. Yamada, Phys. Rev. B **69**, 104111 (2004).
[16] T. Matsunaga, N. Yamada, and Y. Kubota, Acta Crystallogr. Sect. B **60**, 685 (2004).
[17] T. Matsunaga, R. Kojima, N. Yamada, K. Kifune, Y. Kubota, Y. Tabata, and M. Takata, Inorg. Chem. **45**, 2235 (2006).
[18] T. Matsunaga, Y. Umetani, and N. Yamada, Phys. Rev. B **64**, 184116 (2001).
[19] T. Matsunaga and N. Yamada, Jpn. J. Appl. Phys. **43**, 4704 (2004).
[20] L. E. Shelimova, O. G. Karpinskii, P. P. Konstantinov, E. S. Avilov, M. A. Kretova, and V. S. Zemskov, Inorg. Mater. **5**, 451 (2004).
[21] S.-I. Shamoto, N. Yamada, T. Matsunaga, and T. Proffen, Phys. B **385-385**, 574 (2006).
[22] C. W. Sun, J. Y. Lee, and Y. T. Kim, Phys. Stat. Sol. RRL **3**, 254 (2009).
[23] D. Walker, M. A. Carpenter, and C. M. Hitch, Am. Mineral. **75**, 1020 (1990).
[24] D. Walker, Am. Mineral. **76**, 1092 (1991).
[25] D. C. Rubie, Phase Trans. **68**, 431 (1999).
[26] H. Huppertz, Z. Naturforsch. B **56**, 697 (2001).
[27] *TOPAS-Academic*, V. 4.1, Coelho Software, Brisbane, Australia (2007).
[28] *Digital Micrograph 3.6.1*, Gatan Software, Pleasanton, California, USA (1999).
[29] P. A. Stadelmann, Ultramicroscopy **21**, 131 (1987).
[30] *ESVision, 4.0.164*, Emispec Systems Inc., Tempe, Arizona, USA (1994–2002).
[31] P. P. Konstantinov, L. E. Shelimova, E. S. Avilov, M. A. Kretova, and V. S. Zemskov, Inorg. Mater. **37**, 662 (2001).
[32] N. Melnychenko-Koblyuk, A. Grystsiv, St. Berger, H. Kaldarar, H. Michor, F. Röhrbacher, E. Royanian, E. Bauer, P. Rogl, H. Schmid, and G. Giester, J. Phys. Condens. Matter **19**, 046203 (2007).
[33] C. Candolfi, U. Aydemir, M. Baitinger, N. Oeschler, F. Steglich, and Yu. Grin, J. Electron. Mater. **39**, 2039 (2010).
[34] A. Grytsiv, P. Rogl, St. Berger, Ch. Paul, H. Michor, E. Bauer, G. Hilscher, C. Godart, P. Knoll, M. Musso, W. Lottermoser, A. Saccone, R. Ferro, T. Roisnel, and H. Noel, J. Phys. Condens. Matter **14**, 7071 (2002).
[35] G. Rogl, A. Grytsiv, E. Bauer, P. Rogl, and M. Zehetbauer, Intermetallics **18**, 394 (2010).
[36] G. Rogl, A. Grytsiv, E. Bauer, P. Rogl, and M. Zehetbauer, Intermetallics **18**, 57 (2010).